Hydrogen Storage Performances of Nanocrystalline and Amorphous NdMg$_{11}$Ni + x wt% Ni (x = 100, 200) Alloys Synthesized by Mechanical Milling

Yang-Huan Zhang[1,2] · Kai-Feng Zhang[1,2] · Ze-Ming Yuan[1,2] · Peng-Peng Wang[1,2] · Ying Cai[1] · Wen-Gang Bu[2] · Yan Qi[2]

Abstract

Nanocrystalline and amorphous NdMg$_{12}$-type NdMg$_{11}$Ni + x wt% Ni (x = 100, 200) alloys were successfully prepared through ball milling (BM). The microstructures and electrochemical properties were systematically studied to get a more comprehensive understanding of the sample alloys. The maximum discharging capacity could be obtained at only two cycles, indicating that as-milled alloys have superior activation capability. The more the Ni content, the better the electrochemical properties of the as-milled samples. To be specific, the discharge capacities of x = 100 and x = 200 (BM 20 h) samples are 128.2 and 1030.6 mAh/g at 60 mAh/g current density, respectively, revealing that enhancement of Ni content could significantly improve the discharging capacities of the samples. Additionally, milling duration obviously influences the electrochemical properties of the samples. The discharging capacity always rises with milling duration prolonging for the x = 100 sample, but that of the (x = 200) sample shows a trend of first augment and then decrease. The cycling stability of the (x = 100) alloy clearly decreases with extending milling duration, whereas that of the (x = 200) alloy first declines and then augments under the same conditions. In addition, the high rate discharge (HRD) abilities of the sample display the maximal values as milling duration changes. The HRD (HRD = $C_{300}/C_{60} \times 100\%$) values of the as-milled alloys (x = 100, 200) are 80.24% and 85.17%, respectively.

Keywords NdMg$_{12}$ alloy · Mechanical milling · Electrochemical hydrogen storage performance · Dynamic characteristics · Activation energy

1 Introduction

Over the decade the carbon dioxide emission and energy consumption have increased beyond our exception. The large-scale use of new energy vehicles is an effective measure to reduce energy consumption because the energy consumed in the transport sector accounts for a large part of the world's total energy consumption [1]. In fact, as early as in 2009, China has listed Ni-MH cell as the auxiliary power of

hybrid electric vehicle (HEV) as mature products for selling nationwide, which opened up a new area for development of the Ni-MH cell. The excellent electrochemical performances of Ni-MH battery, especially superior discharge capacity, are a precondition for the large-scale successful application of hybrid vehicles [2]. Cao et al. [3] observed that the discharge capacity of this low-cost alloy could reach 311.8 mAh/g and 227.0 mAh/g at a high density of 2C and 5C. The relatively low discharge capacity is an important technical obstacle for some hydrogen storage materials as negative electrode of Ni-MH cells, and even those RE-based AB$_2$- and AB$_5$-type alloys that have been commercialized on a large scale also have not brought satisfactory results. Consequently, it is mandatory to seek for an electrode material with a higher capacity. Mg-based alloys are highly anticipated by researchers in the field of hydrogen vehicles due to their good capacity. The excellent gaseous hydrogen storage capacity of 3.7–6.0 wt% [4] and the theoretical electrochemical capacity (over 1000 mAh/g) [5] make researches play

✉ Yang-Huan Zhang
zhangyh59@sina.com

1 Key Laboratory of Integrated Exploitation of Baiyun Obo Multi-Metal Resources, Inner Mongolia University of Science and Technology, Baotou 014010, China

2 Department of Functional Material Research, Central Iron and Steel Research Institute, Beijing 100081, China

more and more attention to the REMg$_{12}$-type (RE = Nd, Sm and La) Mg-based metallic hydrides. However, there are still unresolved questions such as sluggish dehydriding/hydriding kinetics, comparatively high temperature of dehydrogenation, bad cycle stability and dramatically low electrochemical discharging capacity, which are the main technical obstacles restricting the widespread use of Mg-based alloys in on-board hydrogen storage system and Ni-MH cell system. Therefore, significantly raising the hydrogen storage performances of Mg-based alloys remains one of the major challenges for researchers in the field of hydrogen storage [6–8].

Preparing ultra-fine structure (less than 100-nm range) and adding catalytic materials such as RE metals, transition metal oxides and transition metals [9] are two main methods currently applied by researchers to raise the properties of Mg-based alloys. Some technical methods containing (a) ball milling [10], (b) rapid solidification (RS) [11], (c) equal-channel angular pressing (ECAP) [12] and (d) hydriding combustion synthesis [13], were successfully performed to prepare the Mg-based alloys with different compositions. Melt spinning (MS) and ball milling are universally adopted to obtain nanocrystalline and/or amorphous hydrogen storage alloys with a very uniform element distribution. Wang et al. [14] researched the electrochemical performances of milled MmMg$_{12}$ alloy with Ni powders and found that the initial discharge capacity could be raised to 1200 from 770 mAh/g by enhancing Ni in the alloys from 150 to 200 wt%. The as-spun Mg$_{10}$NiR (R = Nd, Sm and La) alloys display excellent hydrogenation and dehydrogenation kinetics properties, as reported by Zhang et al. [15]. The LaMg$_{11}$Ni alloy prepared by Poletaev et al. [16] exhibits the best hydrogenation kinetics at the highest cooling rate, achieving maximal hydrogen absorption capacity of 5.02 wt% H. Ouyang et al. [17] reported that the AB$_{3.0}$-GN-PM electrode showed excellent activation characteristics, good cycling stability and a high discharge capacity [18]. As is well known to all, Ni plays a very strong catalytic role in the dehydrogenation/hydrogenation of Mg-based alloys and can accelerate the process of amorphization in the alloy. In addition, Ni displays an excellent corrosion resistance in the alkaline solution, significantly improving the electrochemical cycle stability. Hence, NdMg$_{12}$-type NdMg$_{11}$Ni + x wt% Ni (x = 100, 200) alloys with amorphous and nanocrystalline were synthesized successfully by the ball milling, and the electrochemical properties were researched systematically in detail under different Ni contents and milling time.

2 Experimental

The sample NdMg$_{11}$Ni was synthesized via the induction melting method under the protection atmosphere of 0.04 MPa helium preventing magnesium from volatilization. The cast

ingot could be obtained by decanting the molten alloy into a water-cooled copper mold. The as-cast ingots were mechanically broken into small particles and filtered through a 200-mesh sieve. The alloy powder and Ni power were thoroughly mixed according to the mass ratio of chemical formula NdMg$_{11}$Ni + x wt% Ni (x = 100, 200). The mechanically milled was performed under argon atmosphere (preventing the power from being oxidized) at room temperature using the planetary-type mill at the speed of 135 rpm for 5, 10, 20, 40 and 60 h and the Cr–Ni stainless steel balls and the powder in a weight ratio of 35:1. All the preparations of the sample were performed in an Ar-filled glove box to prevent sample oxidation.

Phase identification was further determined via X-ray diffraction (XRD) (D/max/2400 Cu-$K_{\alpha 1}$, 40 kV, 160 mA, 10°/min). The microstructure of the as-milled samples was characterized by high-resolution transmission electron microscopy (HRTEM) (operated at 200 kV, JEM-2100F) equipped with electron diffraction (ED).

The Sieverts apparatus controlled automatically with an accuracy of ± 2 °C was adopted to test the PCT curves and dehydrogenation/hydrogenation kinetics of the samples at 553, 573, 593 and 613 K, respectively. The initial hydrogen pressures for dehydrogenation and hydrogenation are set at 1×10^{-4} MPa and 3 MPa, respectively.

The alloy powders and carbonyl nickel powders were thoroughly mixed in a mass ratio of 1:4 and then cold-pressed (35 MPa) into a circular electrode pellet having total mass of 1 g and a diameter of 15 mm. The electrochemical tests were carried out at 303 K in a tri-electrode open cell consisting of electrolyte (6 M KOH), a working electrode (the metal electrode), Hg/HgO reference electrode as well as sintered Ni(OH)$_2$/NiOOH as the counter electrode. The discharging voltage was defined as the difference value between the reference electrode and the working one. During the discharging/charging cycles, the electrode was initially charged for 15-min resting time and then discharged to a cut-off potential of −0.5 V at the same constant current density.

The electrochemical impedance spectra (EIS) were tested by using the electrochemical workstation (PARSTAT 2273). The EIS was tested at a 50% depth of discharge (DOD), and the amplitude of potential disturbance was 5 mV with the frequency ranging from 10 kHz to 5 mHz. The test parameters of discharging were set 500 mV potential steps for 5000 s at a fully charged state, and the experimental data were collected and analyzed by CorrWare.

3 Results and discussion

3.1 Microstructure characteristics

Figure 1 displays the XRD patterns of the as-cast and milled NdMg$_{11}$Ni + x wt% Ni (x = 0, 100, 200) samples. The

principal crystalline phase NdMg$_{12}$ and subsidiary phase Mg$_2$Ni could be seen in the as-cast alloy. After milling, the diffraction peaks show a trend of merging and a significant broadening, which means the alloy grains are remarkably refined and even form the amorphous structures. In addition, the degree of broadening of the diffraction peak increases significantly with rising the Ni content, manifesting that enhancing Ni content contributes to the formation of glass. The activation energy for the transformation of crystalline to amorphous phase of the REMg$_{12}$ alloys is lower when the Ni content is increased, as stated by Abdellaoui et al. [19]. There are three hydrides, including NdH$_3$, MgH$_2$ and Mg$_2$NiH$_4$, and their production paths are as follows [20]:

$$NdMg_{12} + H_2 \rightarrow MgH_2 + NdH_3. \quad (1)$$

$$Mg_2Ni + H_2 \rightarrow Mg_2NiH_4. \quad (2)$$

In addition, it is worth noting that the lattice expansion and stress caused by the entry of H atoms into the lattice interstitial sites could cause the diffraction peaks of the alloy to be significantly broadened. The amorphous and nanocrystalline structures were still present in saturated hydrogen absorption state, which means that the milled NdMg$_{11}$Ni+x wt% Ni (x=100, 200) samples have a high structural stability.

The bright-field (BF) micrographs of the as-cast and milled samples corresponding to the SAED (the selected area electron diffraction) patterns are shown in Fig. 2. Obviously, the phases of NdMg$_{12}$ and Mg$_2$Ni could be seen in the as-cast sample, which also could be demonstrated by SAED (the selected

area electron diffraction). The x=100 as-milled (20 h) alloy displays a main nanocrystalline structure, while the x=200 as-milled (20 h) alloy exhibits an obvious amorphous and nanocrystalline structures, demonstrating that enhancing Ni content could facilitate the formation of glass, as reported by Teresiak et al. [21]. Furthermore, there are some crystal defects that could be clearly seen in the as-milled samples, such as twin, dislocation and grain boundary. This result is similar to what is described in the literature [22].

3.2 P–C–T curves and thermodynamics

The reaction enthalpy and entropy of the as-milled (20 h) sample alloys could be tested with the help of the pressure composition isotherm (PCI) curves achieved at different temperatures (553, 573, 593, 613 K), as shown in Fig. 3. The pressure plateaus of hydriding and dehydriding of the sample exhibit an evident inclination, and the hysteresis (H_f=ln(P_a/P_d)) becomes larger, indicating that the desorption thermodynamic behavior of the samples could be affected by adding Ni and ball milling. By means of the information in Fig. 3, the Van't Hoff plots of the as-milled samples were obtained from the abovementioned PCI curves, which exhibits good linear relations between ln(P_{H_2}/P_0) and 1/T for all the samples. Furthermore, the entropy ΔS and enthalpy ΔH of the hydriding and dehydriding processes could be readily determined from Van't Hoff equation [23]:

$$\ln\left(\frac{P_{H_2}}{P_0}\right) = \frac{\Delta H}{RT} - \frac{\Delta S}{R}. \quad (3)$$

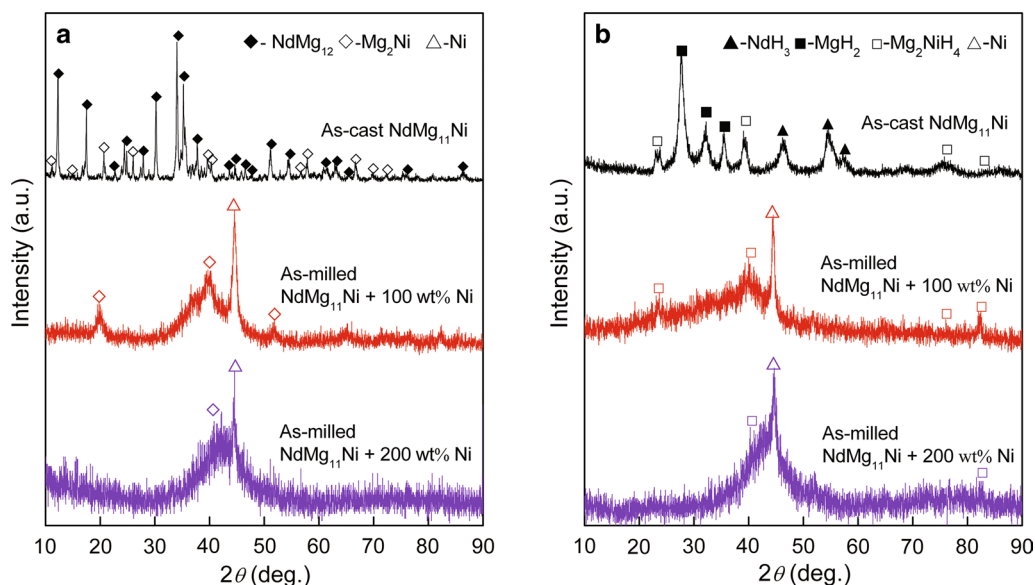**Fig. 1** XRD profiles of the as-cast and milled (20 h) NdMg$_{11}$Ni+x wt% Ni (x=0, 100, 200) alloys before and after hydriding: **a** before hydriding; **b** after hydriding

where P_{H_2} is the equilibrium H pressure (the midpoints corresponding to the 50% of the maximal capacity of the hydriding and dehydriding plateau were used as equilibrium H pressure since the pressure plateaus have an obvious inclination), P_0 means 1 atm, R is the gas constant, and T represents the sample temperature. Table 1 shows the ΔS and ΔH changes of the as-milled alloys. Apparently, increasing Ni content makes the thermodynamic performances, entropy ΔS and enthalpy ΔH, slightly decrease. This result is similar to that reported by Ouyang et al. [24], suggesting that appropriate Ni content helps improve the thermodynamic characteristics. Zhu et al. [25] reported that those components combined with Mg in the composite can catalyze the hydrogenation reaction of Mg.
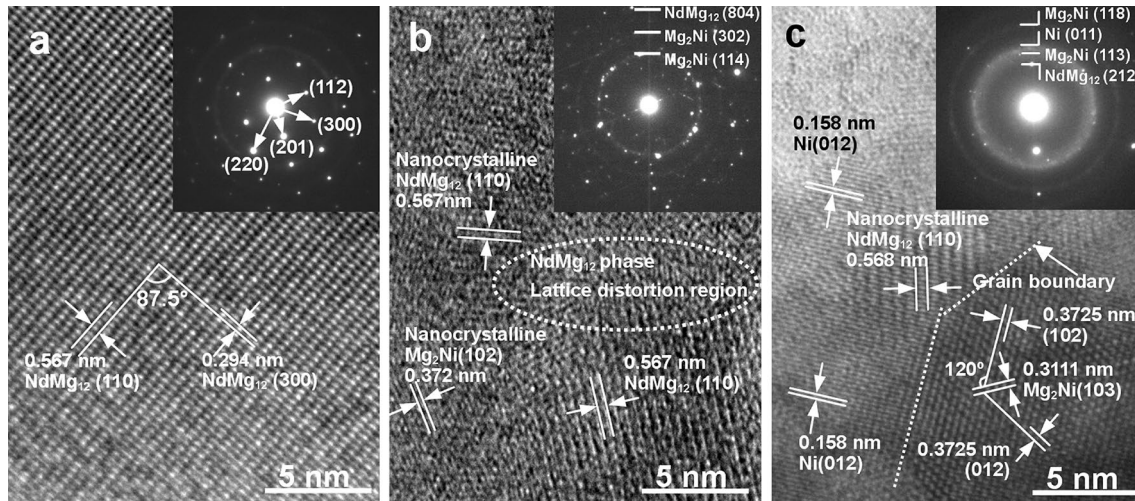

Fig. 2 TEM micrographs and ED patterns of the as-cast and milled (20 h) NdMg$_{11}$Ni + x wt% Ni ($x = 0$, 100, 200) alloys: **a** $x = 0$, as-cast; **b** $x = 100$, milling for 20 h; **c** $x = 200$ milling for 20 h
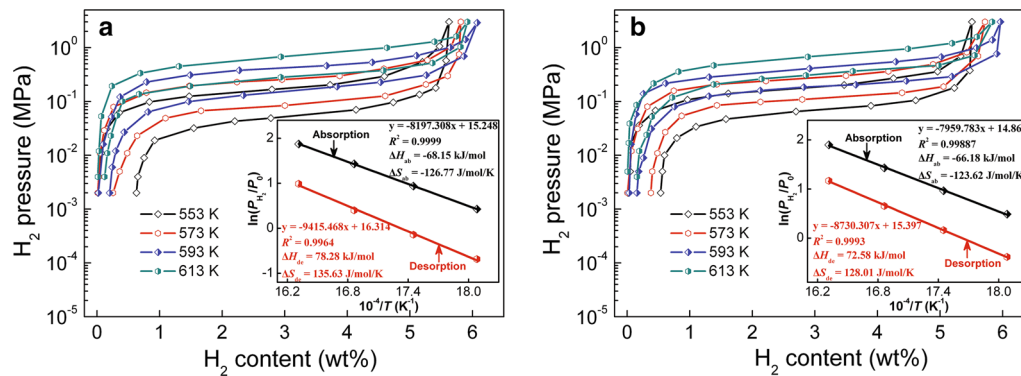

Fig. 3 PCT curves of the as-milled (20 h) NdMg$_{11}$Ni + x wt% Ni ($x = 100$, 200) alloys in the temperature range of 553-613 K and Van't Hoff plots for hydrogen absorption/desorption of the alloys: **a** $x = 100$; **b** $x = 200$

Table 1 Enthalpy and entropy change of as-milled alloys obtained from the Van't Hoff plots	Samples: NdMg$_{11}$Ni + x wt% Ni	Absorption		Desorption	
		ΔH (kJ/mol)	ΔS (J/mol/K)	ΔH (kJ/mol)	ΔS (J/mol/K)
	$x = 100$	−68.15	−126.77	78.28	135.63
	$x = 200$	−66.18	−123.62	72.58	128.01

3.3 Electrochemical Hydrogen Storage Performances

3.3.1 Activation Capability, Discharging Capacity and Discharging Potential Characteristics

Activation capability is a crucial indicator to measure the quality of alloy electrode. The smaller the numbers of discharge/charge cycle required for the battery to reach its maximal discharging capacity, the better the activation property of the electrodes. The evolutions of cycles with the discharge capacity of the sample are presented in Fig. 4. Up to two discharging/charging cycles are required to make the as-milled alloys reach their maximal discharge capacity, which demonstrates that the alloys have good activation performance. In addition, ball milling time is also a key factor affecting the discharge capacity of the samples. The milling duration dependence of the discharging capacities of the as-milled samples is displayed in Fig. 5. The maximal discharging capacity of the x = 200 as-milled sample (20 h) is 1030.6 mAh/g, which is significantly higher 128.2 mAh/g of x = 100 as-milled sample (20 h), at discharge current density of 60 mAh/g. This manifests that the discharging capacity of the milled sample could be obviously improved by enhancing Ni content. In the meantime, we also note that the discharging capacity of the as-milled alloy (x = 100) shows a monotonously increasing trend as prolonging milling duration, which means that the discharging capacity enhances from 39.0 to 164.8 mAh/g when milling time increases from 5 to 60 h. However, the discharging capacity of x = 200 alloy shows a trend of first augment and then decreases with prolonging milling duration, which is different from the trend of x = 100 alloy.

The stability of output power is one of significant indicators for evaluating battery performance. We can use the discharging potential curves of the sample electrodes to evaluate the stability of the battery output power. To be specific, if the discharging potential platform is more horizontal and
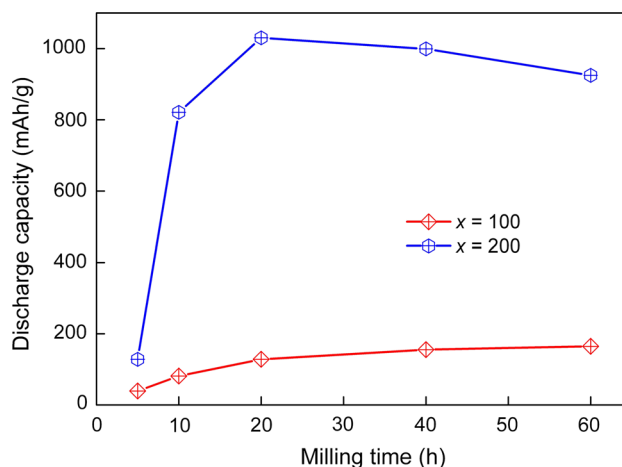
Fig. 5 Variation of the discharge capacity of the as-milled NdMg$_{11}$Ni+x wt% Ni (x=100, 200) alloys with milling time

longer, the discharging potential characteristics of the electrode will be better. The discharging potential curves of the sample alloy electrodes are displayed in Fig. 6 with 60 mA/g current density. As was expected, the milling time can dramatically influence the discharging potential characteristics of the samples. As considered by Lai et al. [26], the internal resistance of the battery, which is closely related to the discharge potential, is the primary factor determining the H diffusion in alloy and the diffusion coefficient increases with the decrease in internal resistance.

Some theoretical elucidations can explain the above test findings. Firstly, the positive action of the addition of Ni on the discharge capacity could be justifiably attributed to its superior corrosion resistance and electrocatalytic activity. As is well known, the elements Mg and Nd that could be oxidized easily are able to form and grow a hydroxide layer and/or magnesium oxide on the electrode surface, which could enhance the interface electronic resistance and lead to sluggish kinetics and low discharge capacity. The corrosion
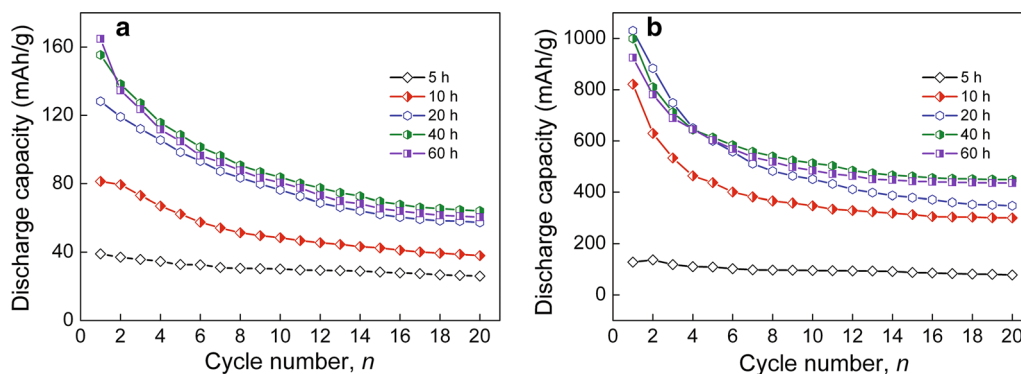
Fig. 4 Evolution of the discharge capacity of the as-milled NdMg$_{11}$Ni+x wt% Ni (x=100, 200) alloys with cycle number: **a** x=100; **b** x=200
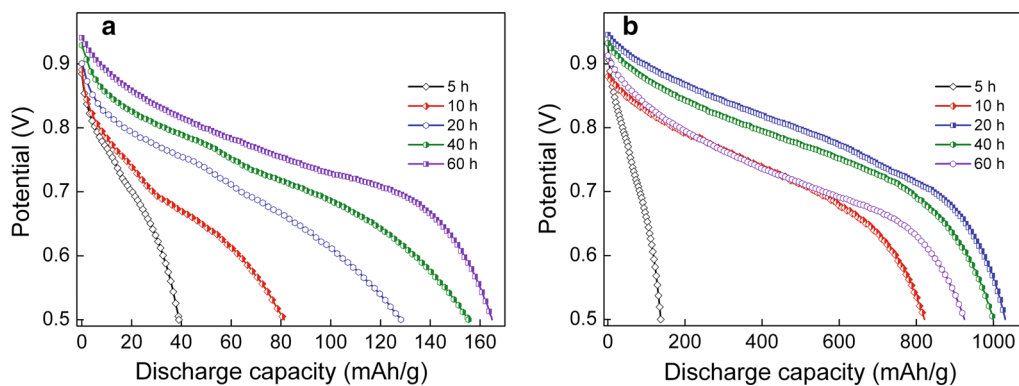
Fig. 6 Discharge potential curves of the as-milled $NdMg_{11}Ni + x$ wt% Ni ($x = 100, 200$) alloys: **a** $x = 100$; **b** $x = 200$

resistance could be improved due to the addition of Ni, hence improving cycle stability and discharge capacity. In addition, the cold welding of alloy powders and Ni powders caused by mechanical ball mill can reduce the hydride stability and enhance the discharging capacity by forming the metallic Ni nanocrystals through alloy matrix with highly dispersed [27]. Presently, we discuss the impact of milling duration on the discharge capacity. The nanocrystalline structure produced by ball milling may be a major reason of the increased discharge capacity, since the H concentration in the grain interior regions and amorphous regions is much lower than that in the grain boundary [28]. Moreover, compared to polycrystalline nickel, H atoms are more easily adsorbed on the nanocrystalline nickel surface, which facilitates the reaction of the hydrogen dissociation and brings on an enhancement in the capacity of an electrode [29]. Kumar et al. [30] confirmed that ultra-fine structure (less than 100-nm range) can make the dehydrogenation temperature of Mg_2Ni alloy decline by 100 K, namely from 573 to 473 K. Lass et al. [31] considered that reducing particle size down to small enough through mechanical milling can significantly enhance the thermodynamics of the hydrogenation and dehydrogenation reactions. The slight reduction in the capacity of ($x = 200$) alloys milled for more than 20 h manifests that the longer milling duration is harmful to the discharge capacity, which could be put down to the formation of the amorphous as it is well known that the nanocrystalline structures are capable of storing more hydrogen than amorphous microstructures.

3.3.2 Electrochemical Cycle Stability

The cycling stability serves as a crucial indicator to evaluate the property of negative material. Here, the cycling stability of the sample electrode could be represented by capacity retaining rate (S_n) with the expression of $S_n = C_n/C_{max} \times 100\%$, where C_{max} represents the maximal discharging capacity and C_n stands for the discharging capacity at the nth discharging/charging cycling at 300 mA/g

current density, respectively. The relationships between the S_n values of the milled $NdMg_{11}Ni + x$ wt% Ni ($x = 100, 200$) alloys with cycling numbers are depicted in Fig. 7. Obviously, with the milling duration increases, the degradation rate of discharging capacity enhances sharply, showing that prolonging milling duration gives a passive influence on the cycling stability of the samples. To straightly display the influence of milling duration on the cycling stability, the relationships between the S_{20} ($n = 20$) values of the samples and milling duration are exhibited in Fig. 8. The different changing tendencies of the S_{20} values of the milled samples with milling duration could be observed. The S_{20} value of the $x = 100$ sample invariably decreases with milling duration prolonging, while that of the $x = 200$ alloy first declines and then augments. It has come to light that the primary cause of resulting in rapid degradation rate of discharging capacity is that Mg was heavily corroded in the KOH solution, followed closely by formation of $Mg(OH)_2$ layer on the alloy surface [32]. Since the intergranular corrosion is unavoidable, the negative effect of the ball milling is more likely to be related to the formation of the nanocrystalline structures and the generation of lattice strains. Increasing the milling time (more than 20 h) can lead to more amorphous phase inside the alloy, because the amorphous structure could enhance the corrosion resistance of the sample in alkaline solution, so that the cycling stability of $x = 200$ alloy could be improved.

3.3.3 Electrochemical Kinetics

The ability to maintain a superior discharge capacity in the process of the charging and discharging cycles at high current density is a precondition for the extensive applications of Ni–MH battery, particularly power battery. The high rate ability (HRD) is a quantitative characterization of the electrochemical kinetics of the electrode, which is defined as: $HRD = C_i/C_{60} \times 100\%$. C_i and C_{60} in the definition stand for the maximal discharging capacity under different current
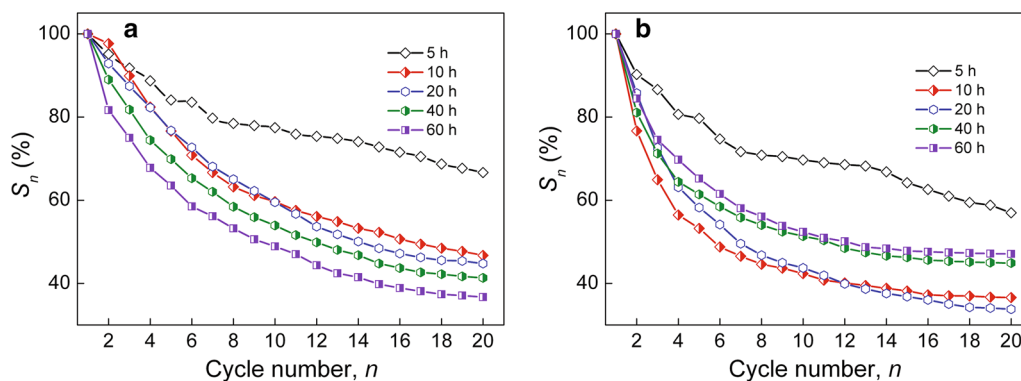
Fig. 7 Variation of the capacity retaining rate (S_n) of the as-milled NdMg$_{11}$Ni+x wt% Ni (x=100, 200) alloys with cycle number: **a** x=100; **b** x=200
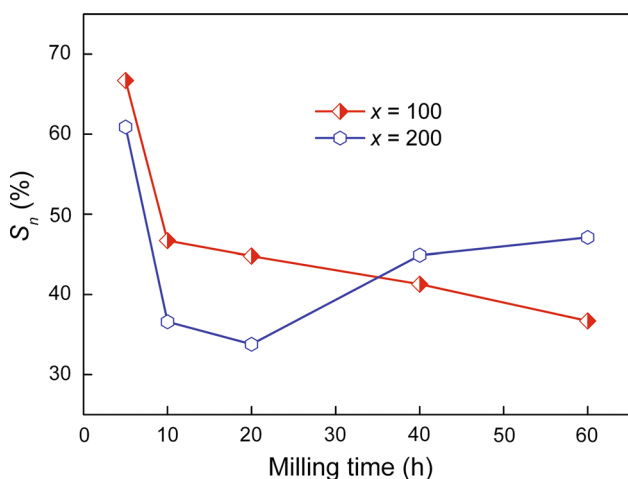

Fig. 8 Variation of the capacity retaining rate (S_{20}) of the as-milled NdMg$_{11}$Ni+x wt% Ni (x=100, 200) alloys with milling time

density, respectively. The subscripts i and 60 are the different condition parameters, representing the current density at charging–discharging cycle. The numerical correspondences between the current density with HRDs of the alloys are displayed in Fig. 9, from which it could be found that the HRDs of the milled samples decrease obviously with growing of current density. For exhibiting the influence of milling time on HRDs, it takes 300 mA/g (i=300 mA/g) current density as a standard, and thus, the variation in function of the HRDs with milling duration can be established, as described in Fig. 9. The HRDs do not always increase monotonously with increasing the milling time but show a tendency of augmenting first and then decrease. For the different Ni content alloys, the milling times corresponding to the maximal HRD value are different, namely 80.24% for the as-milled (20 h) x=100 sample and 85.17% for the as-milled (40 h) x=200 sample, which is in close proximity to the RE-based AB$_5$-type alloy electrodes in possession of acknowledged exceptional kinetics performance.

The HRD is considered to be principally depended on the ability of H diffusion and the surface charge-transfer rate [33]. Hence, we need to explore the influence of the changes in milling duration on the above two factors, which further reveals the intrinsic mechanism that causes the changes in electrochemical kinetics. First, we can
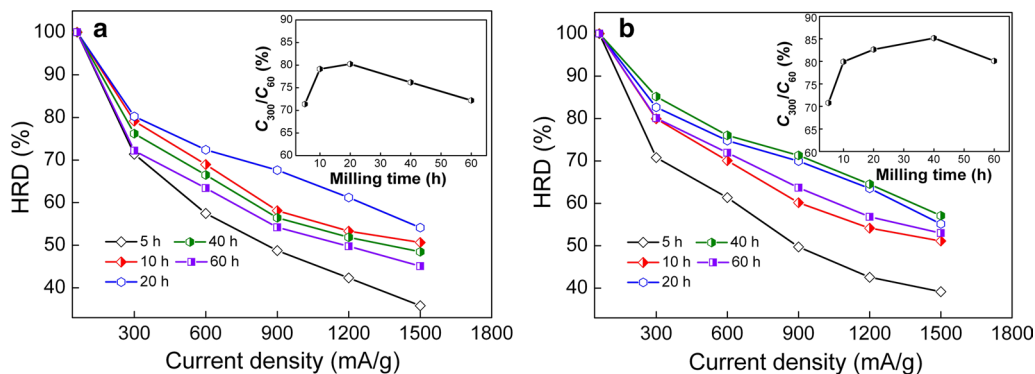

Fig. 9 Evolution of the HRDs of the as-milled NdMg$_{11}$Ni+x wt% Ni (x=100, 200) alloys with current density: **a** x=100; **b** x=200

obtain H diffusion coefficient, as displayed in Fig. 10. By using the White's model [34] and the slope obtained by fitting the linear part of the curves, the diffusion coefficient of the H could be easily computed based on the following formula:

$$\log i = \log\left(\pm\frac{6FD}{da^2}(C_0 - C_s)\right) - \frac{\pi^2}{2.303}\frac{D}{a^2}t. \tag{4}$$

$$D = -\frac{2.303a^2}{\pi^2}\frac{d\log i}{dt}. \tag{5}$$

where i, a, d, t, C_0, D and C_s are the diffusion current density (A/g), radius of the alloy particles (cm), the alloy density (g/cm^3), the discharge duration (s), the initial H concentration (mol/cm^3), the H diffusion coefficient (cm^2/s) and the H concentration (mol/cm^3), respectively. The D values obtained from Eq. (5) as functions of the milling duration are inserted in Fig. 10. Apparently, the D values display a trend of first

growth and then decline as the milling duration prolonging. Concerning charge-transfer rate, it is adopting the model suggested by Kuriyama et al. [35] to evaluate by measuring the electrochemical impedance spectrum (EIS). Figure 11 presents the representative EIS curves at 303 K. Evidently, each EIS can be divided into three portions: high-frequency region, middle-frequency region and low-frequency region which exactly interprets the process of electrode electrochemical. Among them, the smaller semicircle which located in the high-frequency part is the contact resistance between the conductive material and the alloy powder, and surface charge-transfer resistance (R_{ct}) corresponds to the larger one which located in the middle-frequency part. At last, the Warburg impendence corresponds to the straight line located in the low-frequency part. R_{ct} values could be acquired according to the equivalent circuit (see Fig. 11a) by making use of the fitting program Z-View, and the relationship between the R_{ct} value and the milling duration is built, as described in Fig. 11b. According to Kuriyama et al. [35], the R_{ct} value
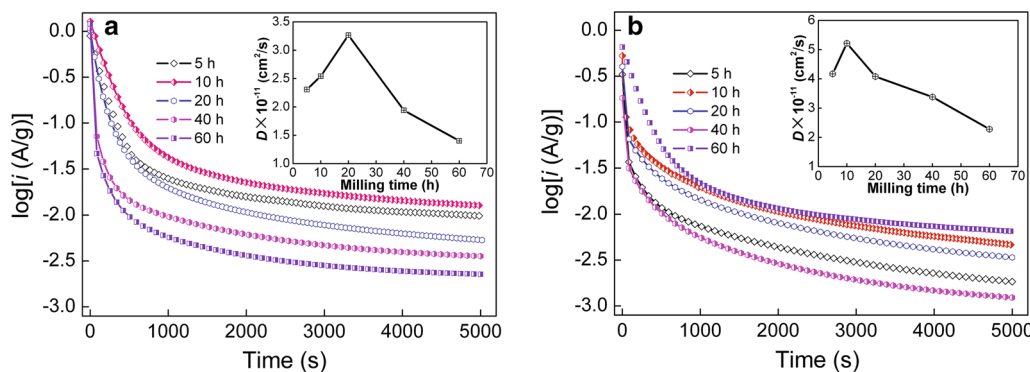

Fig. 10 Semilogarithmic curves of anodic current vs. time responses of the as-milled NdMg$_{11}$Ni + x wt% Ni (x = 100, 200) alloys: **a** x = 100; **b** x = 200
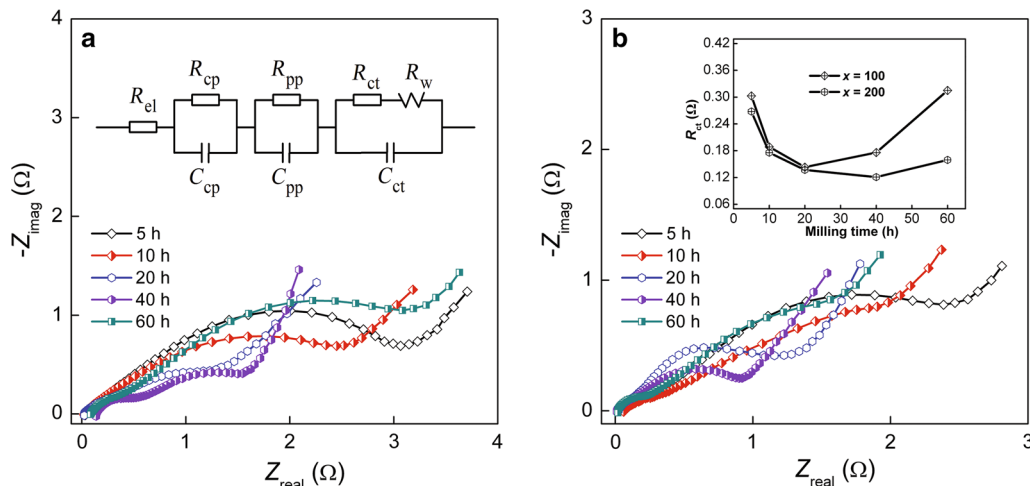

Fig. 11 EIS of the as-milled NdMg$_{11}$Ni + x wt% Ni (x = 100, 200) alloys: **a** x = 100; **b** x = 200

depends essentially on both the reaction area and surface reactivity of the alloy. And the surface electrochemical reactivity could be evaluated with apparent activation enthalpy $\Delta_r H^*$, which could be gained by the subsequent formulae:

$$\ln\left(\frac{T/R_{ct}}{K/\Omega}\right) = C_0 - \frac{\Delta_r H^*}{RT} \qquad (6)$$

where the charge-transfer resistance of electrodes is expressed as R_{ct}, the gas constant is expressed as R, temperature of the sample is expressed as T, and a constant in which the surface area is included is expressed as C_0, respectively. The EIS curves of the milled (20 h) samples were measured at the temperatures of 303, 313 and 323 K, as depicted in Fig. 12. The graph of $\ln(T/R_{ct})$ versus $1/T$, called Kuriyama plots, can be found with the aid of the data of EIS curves and the logarithmic transformation of Eq. (4), as inserted in Fig. 12. The $\Delta_r H^*$ value could be derived from the slope of the Kuriyama plots. The $\Delta_r H^*$ of the milled (20 h) alloys ($x = 100, 200$) is 17.64 and 16.70 kJ/mol, respectively. It could be seen that the $\Delta_r H^*$ values of the samples show a trend of decline first and then increase with the milling duration extending, as depicted in Fig. 12. By contradistinguishing the change tendencies of the HRD and $\Delta_r H^*$ value with the milling duration displayed in Figs. 9 and 13, it could be found that the maximal HRD values and the minimum $\Delta_r H^*$ values of the milled samples ($x = 100, 200$) correspond to one same milling duration, indicating that the electrochemical kinetics of the samples is primarily controlled by the surface charge-transfer ability. Hence, the reduction of activation enthalpy $\Delta_r H^*$ is the cause of the increased HRD by prolonging milling duration and enhancing Ni content.

It could be inferred that increasing milling duration has a dual influence on the electrochemical kinetics of the alloys, which includes both favorable and harmful
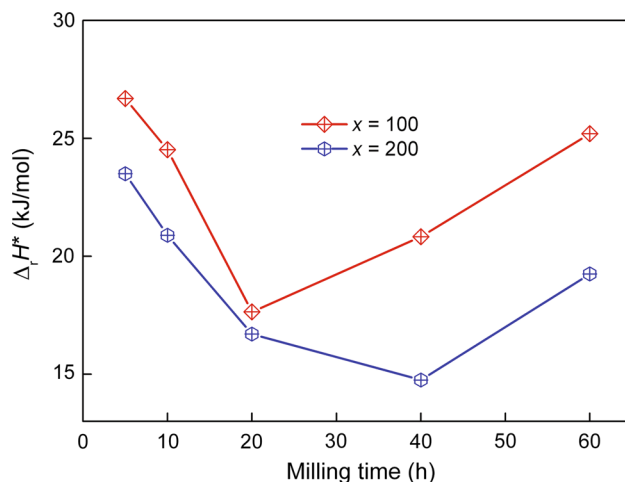
Fig. 13 Evolution of the activation enthalpy $\Delta_r H^*$ values of the as-milled NdMg₁₁Ni + x wt% Ni ($x = 100, 200$) alloys with the milling time

effects. Fundamental modifications on the surface state and a significant reduction in the particle size of the alloy powder are two most likely factors that cause the electrochemical kinetics to improve in a favorable direction. The surface state modification, particularly a large number of crystal defects, can expedite the H diffusion rate and charge-transfer rate. A further reduction in particle size increases the interface area between the electrolyte and the sample particles. The amorphous phase produced ball milling can greatly hinder the pulverization process of the sample particles during the cycles of charging/discharging [36], which reduces usable fresh surface of the sample electrode, thus impairing charge-transfer rate and H diffusion ability.
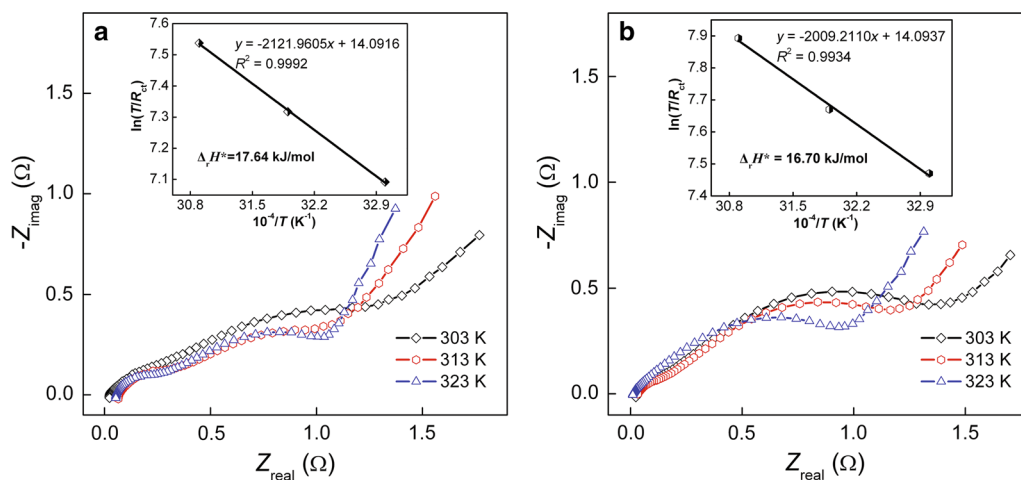
Fig. 12 EIS of the as-milled (20 h) NdMg₁₁Ni + x wt% Ni ($x = 100, 200$) alloys at various temperatures: **a** $x = 100$; **b** $x = 200$

4 Conclusions

(1) The NdMg$_{11}$Ni + x wt% Ni (x = 100, 200) alloys with amorphous and nanocrystalline structures were successfully prepared by ball milling. Enhancing Ni content could promote the formation of glass. Also, it causes a slight decline in the thermodynamic properties, i.e., entropy ΔS and enthalpy ΔH.

(2) The as-milled samples possess superior activation capability, and the maximal discharging capacity can be obtained through at most two discharging/charging cycles. With the enhancement of Ni content, the electrochemical characteristics of the samples are greatly ameliorated. More specifically, enhancing Ni content from 100 to 200 wt% enables the discharging capacity of the milled samples (20 h) to be enhanced from 128.2 to 1030.6 mAh/g. The HRDs of the milled samples have the maximal values as milling duration changes, namely 80.24% for the as-milled (20 h) x = 100 alloy and 85.17% for the as-milled (40 h) x = 200 alloy.

(3) With the increase in milling time, the alloys possess the optimum electrochemical kinetic properties which correspond to the lowest $\Delta_r H^*$ values. Hence, it could be inferred that the charge-transfer capacity is a crucial factor determining the electrochemical kinetics of sample alloys.

References

[1] M.H. Enayati, F. Karimzadeh, S. Sabooni, M. Jafari, Acta Metall. Sin. (Engl. Lett.) **28**, 1002 (2015)

[2] L.Z. Ouyang, T.H. Yang, M. Zhu, D. Min, T.Z. Luo, H. Wang, F.M. Xiao, R.H. Tang, J. Alloys Compd. **735**, 98 (2018)

[3] Z. Cao, L.Z. Ouyang, L. Li, Int. J. Hydrogen Energy **40**, 451 (2015)

[4] Y.H. Zhang, W. Zhang, J.L. Gao, Z.M. Yuan, W.G. Bu, Y. Qi, Acta Metall. Sin. (Engl. Lett.) **30**, 1040 (2017)

[5] Y.H. Zhang, Z.M. Yuan, T. Yang, Z.H. Hou, D.L. Zhao, Acta Metall. Sin. (Engl. Lett.) **28**, 826 (2015)

[6] L.Z. Ouyang, Z. Cao, H. Wang, R.Z. Hu, M. Zhu, J. Alloys Compd. **691**, 422 (2017)

[7] L.Z. Ouyang, X.S. Yang, H.W. Donga, M. Zhu, Scr. Mater. **61**, 339 (2009)

[8] L.Z. Ouyang, F.X. Qin, M. Zhu, Scr. Mater. **55**, 1075 (2006)

[9] M.S. El-Eskandarany, E. Shaban, A. Al-Shemmiri, Int. J. Hydrogen Energy **39**, 21097 (2014)

[10] Y.H. Zhang, Z.M. Yuan, W.G. Bu, F. Hu, Y. Cai, D.L. Zhao, Acta Metall. Sin. (Engl. Lett.) **29**, 577 (2016)

[11] T. Spassov, V. Rangelova, N. Neykov, J. Alloys Compd **334**, 219 (2002)

[12] A.M. Jorge Jr., E. Prokofiev, G.F. de Lima, E. Rauch, M. Veron, W.J. Botta, M. Kawasaki, T.G. Langdon, Int. J. Hydrogen Energy **38**, 8306 (2013)

[13] H. Gu, Y.F. Zhu, L.Q. Li, Int. J. Hydrogen Energy **33**, 2970 (2008)

[14] Y. Wang, X. Wang, C.M. Li, Int. J. Hydrogen Energy **35**, 3550 (2010)

[15] Q.A. Zhang, C.J. Jiang, D.D. Liu, Int. J. Hydrogen Energy **37**, 10709 (2012)

[16] A.A. Poletaev, R.V. Denys, J.P. Maehlen, J.K. Solberg, B.P. Tarasov, V.A. Yartys, Int. J. Hydrogen Energy **37**, 3548 (2012)

[17] L.Z. Ouyang, Z.J. Cao, L.L. Li, H. Wang, J.W. Liu, D. Min, Y.W. Chen, F.M. Xiao, R.H. Tang, M. Zhu, Int. J. Hydrogen Energy **39**, 12765 (2014)

[18] L.Z. Ouyang, X.S. Yang, M. Zhu, J.W. Liu, H.W. Dong, D.L. Sun, J. Zou, X.D. Yao, J. Phys. Chem. C **118**, 7808 (2014)

[19] M. Abdellaoui, S. Mokbli, F. Cuevas, M. Latroche, A. Percheron-Guégan, H. Zarrouk, J. Alloys Compd. **356–357**, 557 (2003)

[20] R.V. Denys, A.A. Poletaev, J.K. Solberg, B.P. Tarasov, V.A. Yartys, Acta Mater. **58**, 2510 (2010)

[21] A. Teresiak, A. Gebert, M. Savyak, M. Uhlemann, Ch. Mickel, N. Mattern, J. Alloys Compd. **398**, 156 (2005)

[22] S.P. Wang, W.H. Luo, G. Li, H.B. Li, G.F. Zhang, Acta Metall. Sin. (Engl. Lett.) **54**, 1187 (2018)

[23] H. Falahati, D.P.J. Barz, Int. J. Hydrogen Energy **38**, 8838 (2013)

[24] L.Z. Ouyang, W. Chen, J.W. Liu, M. Felderhoff, H. Wang, M. Zhu, Adv. Energy Mater. **7**, 170029 (2017)

[25] M. Zhu, H. Wang, L.Z. Ouyang, M.Q. Zeng, Int. J. Hydrogen Energy **31**, 251 (2006)

[26] W.H. Lai, C.Z. Yu, Battery Bimon. **26**, 189 (1996)

[27] Y. Wang, Z.W. Lu, X.P. Gao, W.K. Hu, X.Y. Jiang, J.Q. Qu, P.W. Shen, J. Alloys Compd. **389**, 290 (2005)

[28] T. Spassov, L. Lyubenova, U. Köster, M.D. Baró, Mater. Sci. Eng. A **375–377**, 794 (2004)

[29] L.Z. Ouyang, Z.J. Cao, H. Wang, J.W. Liu, D.L. Sun, Q.A. Zhang, M. Zhu, Int. J. Hydrogen Energy **38**, 8881 (2013)

[30] L.H. Kumar, B. Viswanathan, S.S. Murthy, J. Alloys Compd. **461**, 72 (2008)

[31] E.A. Lass, Int. J. Hydrogen Energy **36**, 10787 (2011)

[32] M.V. Simičić, M. Zdujić, R. Dimitrijević, L. Nikolić-Bujanović, N.H. Popović, J. Power Sources **158**, 730 (2006)

[33] X.Y. Zhao, Y. Ding, L.Q. Ma, L.Y. Wang, M. Yang, X.D. Shen, Int. J. Hydrogen Energy **33**, 6727 (2008)

[34] G. Zhang, B.N. Popov, R.E. White, J. Electrochem. Soc. **142**, 2695 (1995)

[35] N. Kuriyama, T. Sakai, H. Miyamura, I. Uehara, H. Ishikawa, T. Iwasaki, J. Alloys Compd. **202**, 183 (1993)

[36] Y.H. Zhang, Z.M. Yuan, T. Yang, Y. Qi, D.L. Zhao, J Solid State Electr. **19**, 1187 (2015)